

WIND-DRIVEN ACCRETION IN PROTOPLANETARY DISKS — II: RADIAL DEPENDENCE AND GLOBAL PICTURE

XUE-NING BAI¹

Institute for Theory and Computation, Harvard-Smithsonian Center for Astrophysics, 60 Garden St., MS-51, Cambridge, MA 02138
Draft version August 15, 2018

ABSTRACT

Non-ideal magnetohydrodynamical effects play a crucial role in determining the mechanism and efficiency of angular momentum transport as well as the level of turbulence in protoplanetary disks (PPDs), which are key to understanding PPD evolution and planet formation. It was shown in our previous work that at 1 AU, the magnetorotational instability (MRI) is completely suppressed when both Ohmic resistivity and ambipolar diffusion (AD) are taken into account, resulting in a laminar flow with accretion driven by magnetocentrifugal wind. In this work, we study the radial dependence of the laminar wind solution using local shearing-box simulations. Scaling relation on the angular momentum transport for the laminar wind is obtained, and we find that the wind-driven accretion rate can be approximated as $\dot{M} \approx 0.91 \times 10^{-8} R_{\text{AU}}^{1.21} (B_p/10\text{mG})^{0.93} M_{\odot} \text{yr}^{-1}$, where B_p is the strength of the large-scale poloidal magnetic field threading the disk. The result is independent of disk surface density. Four criteria are outlined for the existence of the laminar wind solution: 1). Ohmic resistivity dominated midplane region; 2). AD dominated disk upper layer; 3). Presence of (not too weak) net vertical magnetic flux. 4). Sufficiently well ionized gas beyond disk surface. All these criteria are likely to be met in the inner region of the disk from ~ 0.3 AU to about 5–10 AU for typical PPD accretion rates. Beyond this radius, angular momentum transport is likely to proceed due to a combination of the MRI and disk wind, and eventually completely dominated by the MRI (in the presence of strong AD) in the outer disk. Our simulation results provide key ingredients for a new paradigm on the accretion processes in PPDs.

Subject headings: accretion, accretion disks — instabilities — magnetohydrodynamics — methods: numerical — planetary systems: protoplanetary disks — turbulence

1. INTRODUCTION

Jets and molecular outflows are ubiquitous among young stellar objects (YSOs, see Ray et al. 2007 and Arce et al. 2007 for a review). The velocity of the outflow ranges from a few hundred km s⁻¹ for the axial high-velocity component (HVC) that propagate to large distances, to about 10–50 km s⁻¹ for the so-called low-velocity component (LVC) that is more extended (Hirth et al. 1997; Pyo et al. 2003). The outflow is strongly collimated at large distance (~ 1000 AU scale), with typical opening angle of just a few degrees, while large opening angles (20–30°) are inferred at scales of 10 AU or less (Woitas et al. 2002; Hartigan et al. 2004). It has been well established that outflow is associated with the accretion phenomenon, with the mass outflow rate on the order of a tenth of the mass accretion rate (Cabrit et al. 1990; Hartigan et al. 1995; Cabrit 2007a). The launching and collimation of the jet/outflow in YSOs are almost certainly magnetic in nature (Cabrit 2007b), and most likely magneto-centrifugally driven via the Blandford & Payne (1982) mechanism: outflowing gas launched from the disk can be accelerated along open magnetic field lines centrifugally when the surface poloidal magnetic field is inclined by more than 30° relative to disk normal. The outflow can be gradually collimated beyond the Alfvén point by the magnetic hoop stress from the toroidal field. The accretion-ejection cor-

relation leads to closer studies of the jet/outflow properties in the vicinity the launching region. Using the Hubble Space Telescope, evidence of jet rotation has been identified in a number of sources including DG Tau and RW Aur within the scale of about 100 AU from the star (Bacciotti et al. 2002; Coffey et al. 2004, 2007). Although caveats and alternative explanations do exist (Soker 2005; Cerqueira et al. 2006; Cabrit et al. 2006), the jet rotation observations can be naturally explained as originating from a magnetic outflow. Based on the conservation laws for axisymmetric magnetic outflows, the location of the jet-launching region can be inferred (Anderson et al. 2003), where it was found that the LVC wind in these sources is likely to originate from an extended region in the disk from less than 1 AU to a few AU (Anderson et al. 2003; Coffey et al. 2004, 2007). The launching region of the HVC is not directly constrained due to the resolution limit, but is likely to be located further inward, and may involve an X-wind (Shu et al. 1994; Shang et al. 2007). Further investigations show that the LVC outflow in these systems carries a substantial fraction (if not all) of the disk angular momentum in the launching region (Chrysostomou et al. 2008; Coffey et al. 2008). These observations reveal that the magnetocentrifugal wind is not only responsible for producing the LVC of the outflow in YSOs, but is also likely to play a dominant role in driving accretion for the inner region of protoplanetary disks (PPDs).

Typical accretion rate from PPDs in T-Tauri systems has been well-established to be about $10^{-8\pm 1} M_{\odot} \text{yr}^{-1}$

xbai@cfa.harvard.edu
¹ Hubble Fellow

(Hartmann et al. 1998). Accretion in PPDs has conventionally been largely attributed to be due to the magnetorotational instability (MRI, Balbus & Hawley 1991). Due to the weak ionization level which introduces non-ideal magnetohydrodynamical (MHD) effects, especially near the midplane region of the inner disk, accretion in the inner region of PPDs was thought to be layered (Gammie 1996), with the MRI-driven accretion proceeding in the better-ionized surface layer termed as the active layer, and a more or less laminar midplane region termed as the dead zone. However, this conventional picture takes into account only the effect of Ohmic resistivity, while weakly ionized gas suffers from two other non-ideal MHD effects, namely the Hall effect and ambipolar diffusion (AD). Assuming Hall effect has a limited impact on the MRI as suggested by simulations (Sano & Stone 2002a,b, although the Hall-dominated regime was not covered in these simulations, Wardle & Salmeron 2012), it was shown that the inclusion of AD dramatically reduces the efficiency of the MRI, making it far insufficient to account for the large accretion rate observed in typical T-Tauri disks (Bai & Stone 2011; Bai 2011a,b; Perez-Becker & Chiang 2011a,b; Mohanty et al. 2013). These results strongly suggest magnetized outflow as a promising alternative to drive disk accretion, in line with observations (Bai 2011a).

In our previous paper (Bai & Stone 2013b, hereafter paper I), we have performed a series of local shearing-box simulations for a local patch of PPD at a fixed radius of $R = 1$ AU that for the first time, included both effects of Ohmic resistivity and AD, with magnetic diffusion coefficients self-consistently determined from a pre-computed look-up table in real simulation time. It was shown first that net vertical magnetic flux is essential for driving rapid accretion (otherwise the MRI operates in an extremely inefficient way due to AD), in which case even the initial field configuration is unstable to the MRI, the system quickly relaxes to a state where the MRI is completely suppressed. This is due to large Ohmic resistivity near the disk midplane, and strong AD in the low-density disk surface where the magnetic field becomes too strong for the MRI to operate in the AD dominated regime (Bai & Stone 2011). Instead of the MRI, the disk launches a strong outflow that is magnetocentrifugal in nature. With a physical wind geometry (i.e., the poloidal field/stream lines bend toward the same direction in the shearing-box), a very weak vertical net flux with midplane plasma $\beta_0 = 10^5$ (ratio of gas pressure to magnetic pressure of the net vertical field) is sufficient to drive rapid disk accretion with accretion rate of a few times $10^{-8}M_{\odot} \text{ yr}^{-1}$. Moreover, accretion is likely to proceed through a thin layer where the horizontal magnetic field changes sign (strong current layer), while the rest of the disk remains static. This layer is offset from disk midplane (at about 3 scale heights) and contains a tiny fraction of disk mass but has large radial drift velocity (up to 0.4 times the sound speed) to carry the accretion mass flux.

The results from paper I is on the one hand surprising that MRI no longer operates in the inner disk and the conventional picture of the MRI-driven layered accretion becomes problematic since AD was not considered. On the other hand, the results lend strong the-

oretical support to the observational results of jet and outflows from YSOs summarized at the beginning of this section. We note that most earlier theoretical work on disk wind from PPDs (e.g., Wardle & Koenigl 1993; Li 1995; Ferreira & Pelletier 1995; Königl et al. 2010; Salmeron et al. 2011) generally conclude that strong net vertical magnetic field of equipartition level at disk midplane is needed for wind launching. This is mostly due to the fact that a constant Elsasser number (characterizing the coupling between gas and magnetic field) profile is assumed across the vertical height of the disk. The results from paper I indicates that with a realistic prescription on the vertical profile of the Ohmic and ambipolar diffusion coefficients, launching of a laminar wind can be achieved with much weaker vertical fields (in fact, equipartition-level magnetic field near the launching point, which is high above the midplane), a result that was noticed (Li 1996; Wardle 1997) but not widely acknowledged.

In Paper I we have focused on the physical properties and the launching mechanism of the newly-found laminar wind solution, obtained at fixed radius of 1 AU in a minimum-mass solar nebular disk (MMSN, Weidenschilling 1977). It remains to explore the radial range where such laminar wind solution exist. Toward smaller radii, the disk becomes hotter and eventually thermal ionization of Alkali species takes place (which essentially removes all non-ideal MHD effects). The laminar wind picture would fail, and the gas dynamics is better described by MRI in the ideal MHD regime. Toward larger radii, the gas in PPDs gradually enters the AD dominated regime due to the low density (beyond ~ 20 AU). It has been predicted that MRI-driven accretion can successfully account for the observed accretion rate (Bai 2011b; Perez-Becker & Chiang 2011b), which was later confirmed in numerical simulations, where again, vertical net magnetic flux turns out to be essential (Bai & Stone 2011; Simon et al. 2013a,b, see Section 5.3 for more discussions).

The main purpose of this paper is to identify the criteria (e.g., radial extent) where the laminar wind solution exists, with main focus on the radial dependence of the wind properties. Based on the discussion above, such laminar wind region must exist in the vicinity of 1 AU, but does not extend to the inner edge of the disk, nor to the AD dominated outer disk. We therefore perform the same simulations as in paper I (but with some minor updates) at different disk radii from 0.3 AU to 15 AU and study the wind properties, especially the role of net magnetic flux on wind-driven accretion, as well as the transition from pure laminar wind toward the radius where MRI starts to set in. Piecing together all the simulations results, a global picture concerning the gas dynamics and evolution of PPDs is ready to be revealed.

This paper is organized as follows. We describe our numerical method, model parameters and simulation diagnostics in Section 2. Simulation results in quasi-1D and 3D are presented in Sections 3 and 4 respectively. In Section 5 we discuss the criteria for the existence of laminar wind solution and propose a new global picture on the accretion process in PPDs, together with concluding remarks.

TABLE 1
LIST OF ALL SIMULATION RUNS.

Run	R (AU)	β_0	Dimension	Section
S-R03-b5	0.3	10^5	quasi-1D	3
S-R03-b6	0.3	10^6	quasi-1D	3
S-R1-b4	1	10^4	quasi-1D	3
S-R1-b5	1	10^5	quasi-1D	3
S-R1-b6	1	10^6	quasi-1D	3
S-R3-b4	3	10^4	quasi-1D	3
S-R3-b5	3	10^5	quasi-1D	3
S-R3-b6	3	10^6	quasi-1D	3
S-R5-b4	5	10^4	quasi-1D	3
S-R5-b5	5	10^5	quasi-1D	3
S-R5-b6	5	10^6	quasi-1D	3
S-R8-b4	8	10^4	quasi-1D	3
S-R8-b5	8	10^5	quasi-1D	3
F-R3-b5	3	10^5	3D	4
F-R3-b6	3	10^6	3D	4
F-R5-b5	5	10^5	3D	4
F-R5-b6	5	10^6	3D	4
F-R10-b4	10	10^4	3D	4
F-R10-b5	10	10^5	3D	4
F-R15-b4	15	10^4	3D	4
F-R15-b5	15	10^5	3D	4

MMSN disk model, X-ray luminosity of $L_X = 10^{30}$ ergs s^{-1} and temperature $T_X = 5$ keV, $0.1\mu\text{m}$ grain with mass fraction of 10^{-4} are assumed for all runs.

2. SIMULATIONS

2.1. Simulation Setup

The methodology adopted in this paper follows exactly from paper I (with minor updates), which we briefly summarize below. Readers should consult the entire Section 2 of Bai & Stone (2013b) for details.

We use the Athena MHD code (Stone et al. 2008) and perform three-dimensional (3D) shearing-box simulations for a local patch of a PPD at some fiducial radius R with Keplerian frequency Ω . Radial, azimuthal and vertical dimensions are described by x , y and z coordinates. The gas is assumed to be isothermal with $P = \rho c_s^2$, where ρ , P and c_s are gas density, pressure and isothermal sound speed respectively. Gas velocity with Keplerian velocity subtracted is denoted by \mathbf{v} . Magnetic field is denoted by \mathbf{B} , and we use the unit where magnetic permeability is 1 (so that magnetic pressure is simply $B^2/2$ and so on). Vertical gravity from the central star is included, hence the simulations are vertically stratified, with disk scale height $H \equiv c_s/\Omega$. In our code unit, we have $\rho_0 = \Omega = c_s = H = 1$, where ρ_0 is the midplane gas density in hydrostatic equilibrium, while physically we consider a MMSN disk at radius R . Unless otherwise noted (only in one of the simulation runs), we use a density floor of $\rho_{\text{floor}} = 10^{-6}$.

Ohmic resistivity and AD are included in the simulations, and we use η_O and η_A to denote Ohmic and ambipolar diffusivities. These diffusivities depends on the number density of all charged species, with η_O being independent of magnetic field strength, while in general $\eta_A \propto B^2$ (with complications in the presence of small/tiny grains, see Figure 1 of Bai 2011b). Their values are obtained by interpolating from a pre-computed look-up table, given the local density and ionization

rate in real simulation time. The look-up table is computed by solving a complex chemical reaction network developed in Bai & Goodman (2009) and Bai (2011a) based on rate coefficients from the UMIST database (Woodall et al. 2007). For chemical composition, we assume solar abundance and $0.1\mu\text{m}$ sized grains with mass fraction of 10^{-4} are included. We do not vary grain abundance for all simulations in this paper, mainly because that it was found in paper I that the properties of the wind is very insensitive to grain abundance (see their Figure 13 and explanations in section 5.3). The ionization rate is obtained based on the horizontally averaged column density to the top and bottom of the simulation box, using standard prescriptions for cosmic-ray and X-ray ionizations, as well as ionization rate due to radioactive decay. Furthermore, we adopt a simplified prescription to mimic the effect of FUV ionization based on the model by Perez-Becker & Chiang (2011b) by assuming some fixed ionization fraction f in the FUV layer. The FUV layer lies in the disk surface within the column density of Σ_{FUV} within which we use Equation (8) of paper I to compute magnetic diffusivities, otherwise the diffusivities are interpolated from the look-up table.

In this work, we have slightly modified the prescriptions of the FUV ionization by assuming two FUV ionization layers due to carbon and sulfur respectively, with a sulfur ionization layer with $f = 10^{-5}$ and $\Sigma_{\text{FUV}}^S = 0.03$ g cm^{-2} and a carbon ionization layer that lies further above with $f = 10^{-4}$ and $\Sigma_{\text{FUV}}^C = 0.003$ g cm^{-2} . This prescription is, of course, still very coarse, while it reflects the fact that the ionization fraction increases with height, and alleviates the computational load by allowing larger time steps for calculations in the outer disk (which is relevant only in our simulations with largest radius, i.e., 15 AU). We emphasize that the details in the prescription of the FUV ionization does not affect the physical picture of MRI suppression and wind launching as discussed in paper I. The role of FUV ionization is mainly to make the gas in the disk surface layer well coupled to the magnetic field (i.e., approximately in the ideal MHD regime).

In this paper, we consider only two parameters, namely, the radial location in the disk R and the net vertical magnetic flux, characterized by $\beta_0 = 2P_0/B_{z0}^2$, the ratio of midplane gas pressure ($P_0 = \rho_0 c_s^2$) to the magnetic pressure of the net vertical field ($B_{z0}^2/2$). All other parameters are fixed as described above. The role played by many of these other parameters, such as grain abundance, the depth of the FUV ionization and disk surface density are already explored in Section 5 of paper I, hence we do not repeat.

We conduct two types of simulation runs with different dimensionalities. The first set of runs are fully three-dimensional (3D), with box size being $4H \times 8H \times 16H$ in (x, y, z) , resolved by $96 \times 96 \times 384$ cells. The box size is generally large enough to fit potential MRI modes and these simulations are necessary to identify the transition from fully laminar region close to 1 AU as studied in paper I to the MRI dominated outer disk region. The second set of runs are quasi-one-dimensional (quasi-1D) similar to those presented in Section 4 of paper I, where the vertical domain size remains the same ($16H$) with

slightly higher resolution (512 cells), while the horizontal domain is shrunk to 4×4 cells (and cells have the same aspect ratio as that in the first set of runs). These simulations will reproduce any 3D simulations when the flow is completely laminar while is computationally much cheaper. They are quasi-1D because a pure 1D run has difficulty to evolve into the final laminar state from initial conditions (paper I). All simulation are initialized with a uniform vertical magnetic field B_{z0} characterized by β_0 and random velocity kicks on top of the hydrostatic equilibrium configuration. In addition, a sinusoidally varying vertical field with amplitude $B_{z1} = 4B_{z0}$ is included to avoid the strong initial transient channel flows. All simulations are run for $1200\Omega^{-1}$ (200 orbits, unless otherwise noted) for adequate extraction of time-averaged quantities.

The list of all simulation runs conducted for this paper is shown in Table 1. The range of radius R is from 0.3 AU up to 15 AU. The quasi-1D simulations focus on the inner region, from 0.3 AU to 8 AU where the laminar wind solution is likely to hold; while the full 3D runs focus on regions further out, from 3AU to 15 AU where MRI may possibly set in. Since the inner boundary of this laminar zone depends on the location where thermal ionization takes place, which requires the detailed study of disk thermodynamics and is beyond the scope of this paper, we simply focus on the radial dependence of laminar wind properties without asking the location of its inner laminar zone boundary. On the other hand, the 3D runs that properly accommodate the MRI modes will help identify outer boundary of the laminar wind zone.

2.2. Diagnostics

Before we present simulation results, we describe the main diagnostics in our simulations. Since all our simulations have net vertical magnetic flux, launching of disk outflow is inevitable². In the case of laminar wind studied in detail in paper I (which also applies to the quasi-1D simulations in our Section 3), we have separated the system into a disk zone containing disk midplane and wind zones at disk surface. The transition from disk zone to wind zone occurs when the azimuthal gas velocity switches from sub-Keplerian to super-Keplerian (i.e., v_y changes sign in our shearing-box simulations). This location is also referred to as the base of the wind, beyond which the magnetocentrifugal mechanism takes place and efficiently accelerates the outflow as it leaves the simulation domain. In 3D simulations where MRI starts to set in but not yet dominant (Section 4), one can still obtain time and horizontally averaged vertical profiles and define the disk and wind zones based on the same criterion. With this definition, the main diagnostics for our simulations include

- The $R\phi$ component of the stress tensor in the disk zone, which is directly related to angular momentum transport in the radial direction. It can be written as the sum of Reynolds (hydrodynamic)

² The properties of disk wind also depend on global field geometry, etc., but the launching of outflow is a local process enabled by the presence of net vertical magnetic flux.

and Maxwell (magnetic) components

$$T_{R\phi} \equiv T_{R\phi}^{\text{Rey}} + T_{R\phi}^{\text{Max}} = \overline{\rho v_x v_y} - \overline{B_x B_y}, \quad (1)$$

where the overline denotes horizontal- (and time-except in Figure 4) average. Vertically integrating $T_{R\phi}$ across the disk zone, one obtains the Shakura-Sunyaev α parameter (Shakura & Sunyaev 1973)

$$\alpha \equiv \frac{\int_{-z_b}^{z_b} T_{R\phi} dz}{c_s^2 \int \rho dz}, \quad (2)$$

where z_b is the location of the base of the wind. Similarly, we use α^{Max} and α^{Rey} to denote contributions from the Maxwell and Reynolds components.

- Location of the base of the wind z_b (where \bar{v}_y switches sign), as well as the location of the Alfvén point z_A , defined as the point where the gas vertical velocity equals the vertical Alfvén velocity $\bar{v}_z = \sqrt{B_z^2/\bar{\rho}}$. Note that in the presence of turbulence, turbulent r.m.s. vertical field is adopted.
- Rate of mass outflow from the top and bottom sides of disk surfaces $\dot{M}_w \equiv |\overline{\rho v_z}|_{\text{top}} + |\overline{\rho v_z}|_{\text{bot}}$. We note that in shearing-box simulations, the value of \dot{M}_w is decreases with increasing box height hence is not well constrained. On the other hand, its dependence on various physical parameters remains meaningful (as discussed in Section 4.5 of paper I).
- The $z\phi$ component of Maxwell stress at z_b , which is directly related to angular momentum transport in the vertical direction. It is defined as

$$T_{z\phi}|_{z_b} = T_{z\phi}^{\text{Max}} \equiv (-B_z B_y)|_{\pm z_b}. \quad (3)$$

Note that the corresponding Reynolds stress is zero at z_b by definition ($v_y|_{\pm z_b} = 0$). As shown in paper I, $T_{z\phi}$ is roughly independent of the simulation box height, hence it can be considered as a robust measure of the wind-driven accretion rate.

- The Elsasser numbers for Ohmic resistivity and AD, defined as

$$\Lambda \equiv \frac{v_A^2}{\eta_O \Omega}, \quad Am \equiv \frac{v_A^2}{\eta_A \Omega}, \quad (4)$$

respectively, where $v_A^2 = B^2/\rho$ is the Alfvén velocity. Note that $\Lambda \propto B^2$, while Am is largely independent of B since in general $\eta_A \propto B^2$. The Elsasser numbers characterize the relative importance between the non-ideal MHD terms and the inductive term, and non-ideal MHD terms dominate when $\Lambda, Am < 1$. In particular, the MRI will be suppressed when $\Lambda < 1$, and when magnetic field is too strong at a given Am (see Figure 16 of Bai & Stone 2011). Although the Hall term is not included in our simulations, we do compute the Hall Elsasser number $Ha \equiv v_A^2/\eta_H \Omega$ for discussion purposes.

Assuming steady state accretion, the accretion rate can be estimated as

$$\begin{aligned} \dot{M} &= \frac{2\pi}{\Omega} \int_{-z_b}^{z_b} dz T_{R\phi} + \frac{4\pi}{\Omega} R T_{z\phi} \Big|_{-z_b}^{z_b} \\ &= \frac{2\pi}{\Omega} \alpha c_s^2 \Sigma + \frac{8\pi}{\Omega} R |T_{z\phi}|_{z_b}, \end{aligned} \quad (5)$$

where the two terms correspond to radial transport and vertical transport respectively, and it is assumed that the outflow has a physical geometry so that $T_{z\phi}|_{z_b} = -T_{z\phi}|_{-z_b}$. Plugging in the numbers for a MMSN disk, we further have

$$\dot{M}_{-8} \approx 0.82 \left(\frac{\alpha}{10^{-3}} \right) R_{\text{AU}}^{-1/2} + 4.1 \left(\frac{|T_{z\phi}|_{z_b}}{10^{-4} \rho_0 c_s^2} \right) R_{\text{AU}}^{-3/4}, \quad (6)$$

where \dot{M}_{-8} is the accretion rate normalized to $10^{-8} M_{\odot} \text{yr}^{-1}$.

In many 3D simulations, the systems become prone to the MRI. To quantify the effectiveness of turbulence, we further evaluate the $R\phi$ component of the turbulent Maxwell and Reynolds stresses in all 3D runs, which are obtained by subtracting contributions due to large-scale magnetic field and velocity field

$$\begin{aligned} T_{R\phi, \text{turb}} &\equiv T_{R\phi, \text{turb}}^{\text{Rey}} + T_{R\phi, \text{turb}}^{\text{Max}} \\ &= (\overline{\rho v_x v_y} - \bar{\rho} \bar{v}_x \bar{v}_y) - (\overline{B_x B_y} - \bar{B}_x \bar{B}_y). \end{aligned} \quad (7)$$

Correspondingly, one can also define α_{turb} for Maxwell and Reynolds components following equation (2).

2.2.1. Symmetry and Strong Current Layer

Symmetry of the solutions has been discussed extensively in Section 4.4 of paper I. Here we briefly summarize the main results. Since curvature is ignored in shearing-box approximation, there is no distinction between radially inward and outward directions. A physical wind picture requires that the outflows from the top and bottom sides of the box bend toward the same direction, or equivalently, the radial and toroidal components of the magnetic field bend toward the same direction. For the quasi-1D solutions obtained in paper I (at 1 AU), it was shown that the bending directions at the top and bottom sides are random, and they are independent, hence there is equal chance to obtain physical and unphysical solutions. The unphysical solutions are smooth, and all three component of the magnetic field remain the same sign throughout the disk, which is said to obey odd- z symmetry. Toroidal field is the dominant component within the disk. The physical wind solution requires the horizontal field to change sign across the disk. If this occurs at the midplane, the solution would obey even- z symmetry. However, simulations show that the flip occurs in a thin layer that is offset from the midplane, forming a strong current layer. This layer carries the entire accretion flow, while other than the flip of horizontal magnetic field, the properties of the outflow are exactly the same as those in the solution with odd- z symmetry.

In paper I, it was also noted that the strong current layer does not seem to be long-lived in 3D shearing-box simulations (see footnote 12 of paper I), and the odd- z symmetry solution (unphysical) is preferred. This fact

is likely due to the limitations of the shearing-box approximation, where curvature is ignored and the vertical domain size is limited³. Recent 2D global disk simulations at least suggest the possible existence of strong current layer offset from the disk midplane (e.g., the kink feature in Figure 13 of Fendt & Sheikhezami 2013, although their simulations involve much stronger magnetic field and rough treatment of microphysics). Still, global simulations in 3D are essential to properly study the behavior of the strong current layer.

Since the properties of the outflow is largely independent of the symmetry of the solution in shearing-box, in this work, we mainly focus on the outflow/wind properties. In particular, for 3D simulations, the large-scale field of all runs end up with odd- z symmetry, hence we do not label their symmetries separately. For quasi-1D simulations, we report the symmetry of the solution (which is random) as “odd” (unphysical) or “even” (physical, despite that the strong current layer is offset from the midplane). For physical solutions, we further characterize the strong current layer by

- Maximum radial velocity $v_{R, \text{max}}^{\text{SC}}$ in the strong current layer. We further use z^{SC} to denote the location where $v_{R, \text{max}}^{\text{SC}}$ is achieved.
- The thickness of the strong current layer h^{SC} , estimated by h^{SC} by

$$h^{\text{SC}} \equiv \frac{\int_{\text{SC}} \rho(z) v_x(z) dz}{\rho(z^{\text{SC}}) v_{R, \text{max}}^{\text{SC}}}, \quad (8)$$

where the integral is performed through the strong current layer, in which we use $v_{R, \text{max}}^{\text{SC}}$ as a characteristic radial velocity.

3. RESULTS: QUASI-1D SIMULATIONS

Most of the quasi-1D simulations settle into pure laminar state with the structure of the solution similar to that described in paper I. Major diagnostics are calculated when full laminar states are reached for each of these runs with results listed in Table 2. In order to study the properties of the strong current layer, for some parameter sets, we conduct the same simulation for more than once with different random seeds to find solutions with both symmetries. They apply to runs S-R1-b6 and S-R3-b5, where we further use “a” and “b” to label solutions with odd- z and even- z symmetries respectively. In addition, we find that the gas density in run S-R03-b6 at vertical boundaries hits the floor value of 10^{-6} , hence we reduce floor value to 10^{-7} in this particular run.

Due to a slightly different treatment of the FUV ionization, we first calibrate our runs S-R1-bx with their counterparts in paper I (S-OA-bx), where $x = 4, 5$ or 6 . Comparing our Table 2 with Table 4 of paper I, we see that all major diagnostic quantities between the two sets of simulations agree very well (mostly within 5%). This

³ Curvature may make the physical wind geometry solution more preferable. Also, disk outflow from real disks is likely weaker than obtained from typical shearing-box simulations due to limited box height (paper I), which may make the strong current layer less susceptible to instabilities.

TABLE 2
RESULTS FOR ALL QUASI-1D SIMULATIONS WITH A LAMINAR WIND.

Run	α^{Max}	$T_{z\phi}^{\text{Max}}$	\dot{M}_w	z_b	z_Λ	Symmetry	$ z^{\text{SC}} $	h^{SC}	$v_{R,\text{max}}^{\text{SC}}$
S-R03-b5	2.71×10^{-4}	7.17×10^{-5}	1.36×10^{-5}	4.51	6.92	Odd	-	-	-
S-R03-b6	4.10×10^{-5}	1.36×10^{-5}	4.67×10^{-6}	5.05	5.98	Odd	-	-	-
S-R1-b4	1.26×10^{-3}	5.87×10^{-4}	8.82×10^{-5}	3.92	7.39	Odd	-	-	-
S-R1-b5	2.37×10^{-4}	1.04×10^{-4}	2.92×10^{-5}	4.61	6.13	Even	3.05	0.13	0.47
S-R1-b6a	2.97×10^{-5}	2.73×10^{-5}	1.08×10^{-5}	4.52	5.36	Odd	-	-	-
S-R1-b6b	2.88×10^{-5}	2.42×10^{-5}	8.95×10^{-6}	4.50	5.50	Even	3.01	0.35	3.5×10^{-2}
S-R3-b4	1.52×10^{-3}	7.92×10^{-4}	1.86×10^{-4}	4.28	6.33	Even	1.98	0.17	0.19
S-R3-b5a	2.02×10^{-4}	2.01×10^{-4}	6.98×10^{-5}	4.17	5.27	Odd	-	-	-
S-R3-b5b	1.66×10^{-4}	1.96×10^{-4}	6.54×10^{-5}	4.11	5.33	Even	1.73	0.80	6.6×10^{-3}
S-R5-b4	1.51×10^{-3}	1.06×10^{-3}	2.83×10^{-4}	4.03	5.80	Even	1.64	0.23	0.11
S-R5-b5	1.81×10^{-4}	2.53×10^{-4}	8.98×10^{-5}	3.92	5.08	Even	1.27	1.25	2.7×10^{-3}
S-R8-b4	1.75×10^{-3}	1.40×10^{-3}	4.11×10^{-4}	3.80	5.33	Even	1.64	0.23	0.13

Note that all numbers above are in code unit ($\rho_0 = c_s = \Omega = 1$). We have conducted runs S-R1-b6 and S-R3-b5 twice labeled with “a” and “b” respectively with different initial random seeds, and their resulting solutions end up with different symmetries. Runs S-R3-b6, S-R5-b6 and S-R8-b5 turn out to be unsteady, hence are not included in this table.

is not surprising since the adopted penetration depth of the FUV ionization are the same ($0.03g \text{ cm}^{-2}$), and the gas behaves closely to ideal MHD within the FUV layer. In general, the introduction of the second the FUV ionization layer on top of the first one has no influence on the properties of the solution for all our quasi-1D runs.

3.1. A Fiducial Example

We pick run S-R3-b5 as a fiducial example to illustrate the laminar wind solution at 3 AU in Figure 1. Here we pick the run with odd- z symmetry (no strong current layer) to be directly compared with its 1 AU counterpart shown in Figure 5 of paper I. The basic properties of between the two solutions are very similar. The disk zone is generally gas pressure dominated, and the magnetic field is dominantly toroidal. The toroidal field profile near the midplane is almost flat, which is because of the excessively large magnetic diffusion that makes the gas and magnetic field effectively decoupled (hence current is not permitted). The vertical gradient of the toroidal magnetic field gives radial current, which generates a Lorentz force in the azimuthal direction. The balance of this force with Coriolis force leads to radial motion in the gas, which bends the poloidal magnetic field. Upon achieving a sufficiently large bending angle ($> 30^\circ$), the wind is effectively launched and accelerated by the magnetocentrifugal mechanism.

Comparison between our Figure 1 with Figure 5 of paper I reveal a few trends about the dependence of the solution on disk radii. First of all, the magnetic diffusion coefficients at disk midplane is substantially reduced at 3 AU relative to those at 1 AU. In particular, the Ohmic resistivity cap and the floor on Am are no longer reached (see the end of Section 2 of paper I). Correspondingly, the magnetically decoupled region (where field lines are straight) shrinks to within $z = \pm 2H$. This means that wind launching process takes place further deeper toward disk midplane. Moreover, AD becomes more dominant at 3 AU. In fact, if we do not consider the Hall effect, then the entire disk is AD dominated (this is partly because magnetic field is strongest at disk midplane). Nevertheless, the Ohmic Elsasser number is still well below 1 at disk midplane, too small for MRI to take place.

Secondly, the FUV ionization, assumed to have a fixed penetration depth in column density, penetrates deeper into the disk, with the FUV ionization front located at about $\pm 4H$ instead of $\pm 4.5H$. As discussed in paper I, deeper penetration depth leads to larger wind mass loss rate (in code unit), as seen from Table 2. Similarly, the base of the wind z_b and the Alfvén point are also located deeper at 3 AU. For all our quasi-1D runs at the inner disk, the addition of the second FUV ionization layers further higher above does not have any impact on the wind solution.

Together, with weaker magnetic diffusion and deeper FUV penetration, we see from Table 2 that the wind at 3 AU is about two times stronger (in code/natural unit) than that at 1 AU in terms of the outflow rate \dot{M}_w , as well as the wind stress $T_{z\phi}^{\text{Max}}$, assuming that the background plasma β_0 to be the same.

3.2. Parameter Dependence

In this subsection we discuss how the wind mass loss rate \dot{M}_w and the wind-driven accretion rate (due to $T_{z\phi}^{\text{Max}}$) depend on net vertical magnetic flux and disk radius. In paper I, we found that at 1 AU, the wind stress $T_{z\phi}$ scales with net vertical flux approximately as $\beta_0^{-0.7}$, and \dot{M}_w scales with net flux approximately as $\beta_0^{-0.5}$. With our new set of simulations at different radii, we update their results with new simulation data shown in Table 2 and plotted on Figure 2.

Clearly, we see that the power-law dependence of \dot{M}_w and $T_{z\phi}^{\text{Max}}$ on the net vertical magnetic flux persists at all radii as long as the laminar wind solution exists. Assuming further a power-law dependence on disk radii in the form of $CR^q\beta_0^{-b}$, where C is a constant, we find the following fitting results using linear regression

$$\frac{\dot{M}_w}{\rho_0 c_s} \approx 3.08 \times 10^{-5} \left(\frac{\Sigma_{\text{MMSN}}}{\Sigma} \right) \left(\frac{R}{\text{AU}} \right)^{0.70} \left(\frac{\beta_0}{10^5} \right)^{-0.46}, \quad (9)$$

$$\frac{T_{z\phi}^{\text{Max}}}{\rho_0 c_s^2} \approx 1.16 \times 10^{-4} \left(\frac{\Sigma_{\text{MMSN}}}{\Sigma} \right) \left(\frac{R}{\text{AU}} \right)^{0.46} \left(\frac{\beta_0}{10^5} \right)^{-0.66}. \quad (10)$$

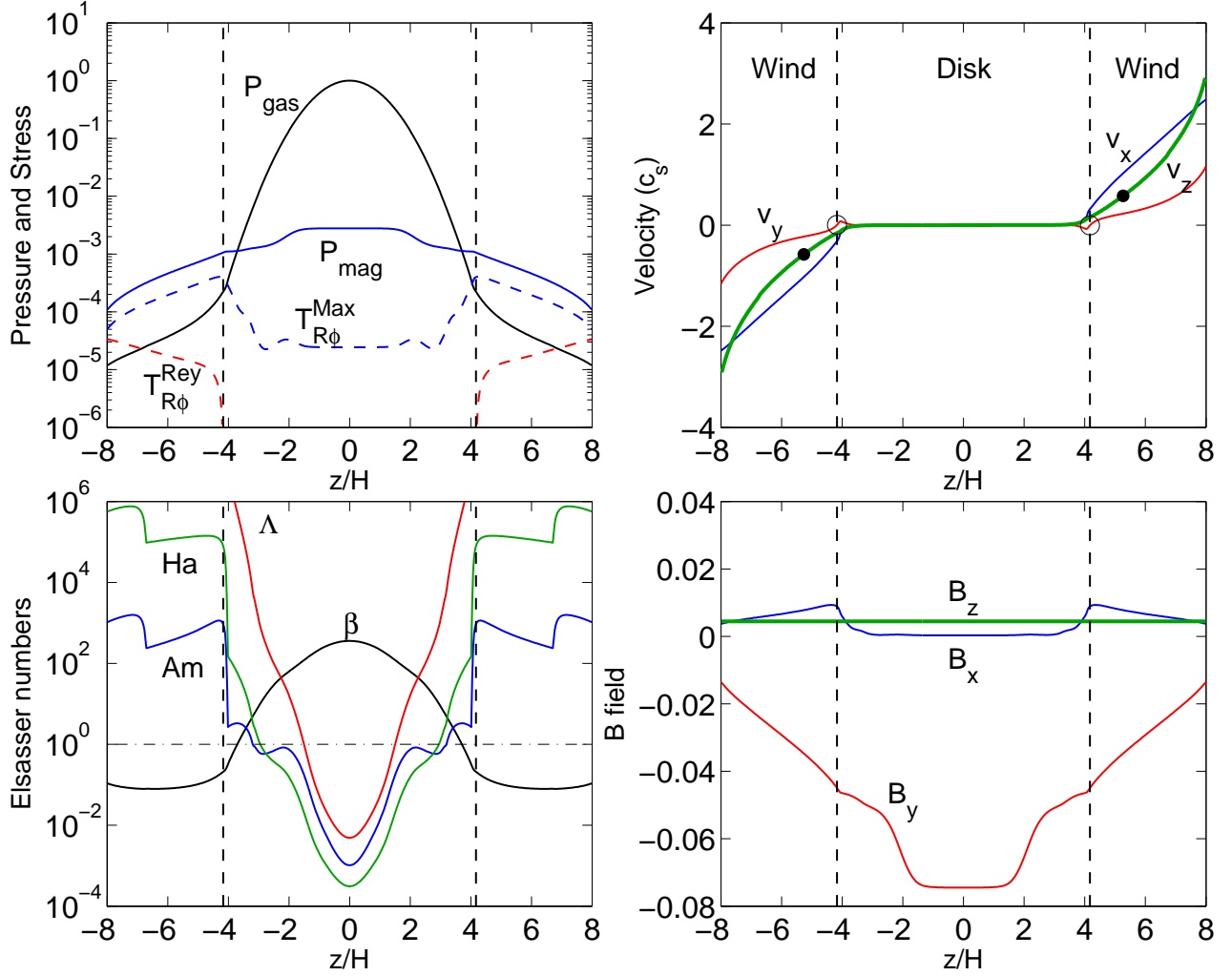


FIG. 1.— Vertical profiles of various quantities in the representative quasi-1D run S-R3-b5 at 3 AU with $\beta_0 = 10^5$ (with odd- z symmetry). Upper left: gas pressure and magnetic pressure, as well as the $R\phi$ component of Maxwell and Reynolds stresses. Lower left: Elsasser numbers for Ohmic resistivity (Λ), Hall term (Ha) and AD (Am), together with $\beta = P_{\text{gas}}/P_{\text{mag}}$. Note that we evaluate Ha for discussion purposes while the Hall effect is not included in the simulations. Upper right: three components of gas velocity, where the bold green curve is for vertical velocity. The Alfvén points are indicated as black dots, while open circles mark the base of the outflow. Lower right: three components of the magnetic field, where the bold green curve is for vertical field. In all panels, the vertical black dashed lines divide the domain into the disk zone (in the middle) and wind zones at the location of the wind base.

Here we have further included a factor $\Sigma_{\text{MMSN}}/\Sigma$, the inverse of disk surface density normalized to the MMSN value (for reasons to be discussed). The fitting results are also plotted in Figure 2, which we see that the above fitting formulas match our simulation results perfectly.

We note that these fitting formulas are derived from local shearing-box simulations of a MMSN disk. We recall from paper I (see their Section 5.4) that the wind mass loss rate \dot{M}_w and wind stress $T_{z\phi}^{\text{Max}}$ in *physical unit* depend only on the *physical strength* of the net vertical field. Therefore, to apply the formulas to disks with different surface densities, two measures should be taken: 1). The factor of $\Sigma_{\text{MMSN}}/\Sigma$ is included on the right hand side of the formulas because the normalization factors on the denominator of the left hand side contain $\rho_0 \propto \Sigma$. 2). One must interpret β_0 as the ratio of midplane gas pressure of a MMSN disk to the magnetic pressure of the net vertical field. In other words, for a hypothetical disk with $\Sigma_1 = N\Sigma_{\text{MMSN}}$ and vertical plasma β_1 , one should

set $\Sigma = \Sigma_1$ and $\beta_0 = \beta_1/N$ in the formula above.

For wind stress $T_{z\phi}^{\text{Max}}$, it was found in paper I that its value is very insensitive to vertical box height. Therefore, the value obtained from shearing-box simulations provides a robust estimate of wind-driven accretion rate from Equation (5).

The wind mass loss rate \dot{M}_w , unfortunately, is not well determined determined from shearing-box simulations. As discussed in paper I, \dot{M}_w roughly depends inversely on the vertical size of the simulation domain L_z , and a physical value might be achieved with $L_z \sim 2R$. Since $H/R \ll 1$ in PPDs, our Equation (9) tend to significantly overestimate the wind mass loss rate in real disks. A possible estimate of the true wind mass loss rate may be obtained by multiplying a factor of $8H/R$ on the right hand side of Equation (9), since the box height in all our simulations is $L_z = 16H$. It would be straightforward to apply the value of H/R from MMSN or other disk models into the formula, but we do not proceed further

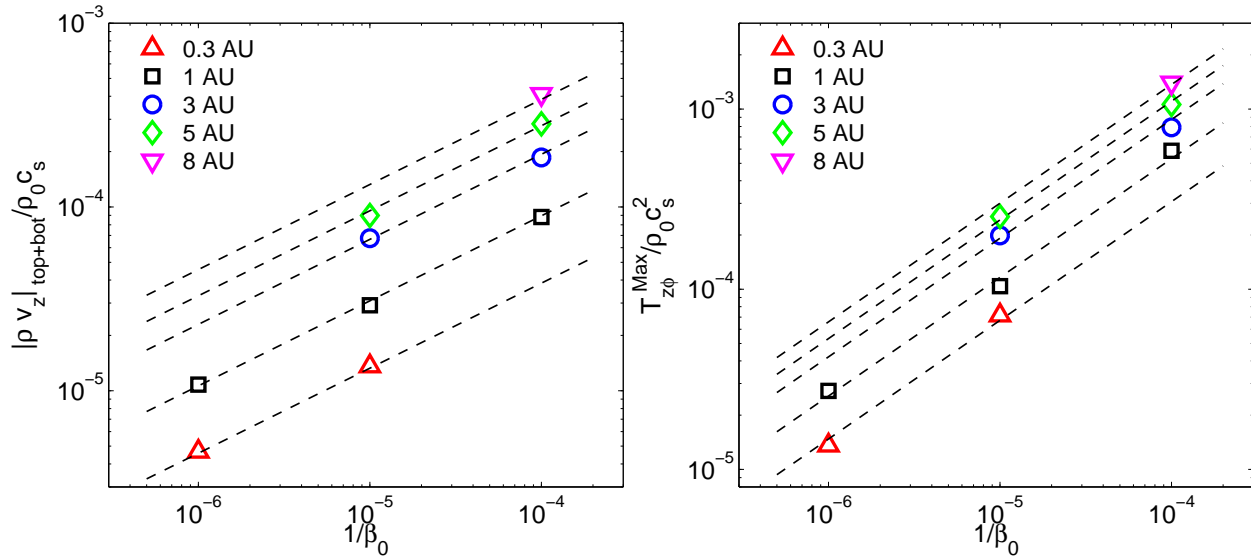


FIG. 2.— The wind mass loss rate \dot{M}_w (left) and wind stress $T_{z\phi}^{\text{Max}}$ (right) as a function of net vertical magnetic flux (characterized by β_0) measured from all our quasi-1D simulations with a laminar wind. Different symbols correspond to simulations at different radii, and dashed lines are fitting results for each radii, using equations (9) and (10). All quantities are in code units, while see discussions in Section 3.2 for caveats.

here since such estimate is very speculative. Future work with global simulations are needed to provide a definitive answer.

The dimensionless form of the fitting formulas above have quantified the radial dependence of wind properties. The indices on β_0 is slightly different but consistent with those reported in paper I. In particular, they confirm the trend discussed in the previous subsection that relatively stronger wind (in code unit) is launched at larger radii due to weaker magnetic diffusion and deeper FUV penetration.

For a MMSN disk, we note that the index on R in the fitting formula (10) is smaller than $3/4$. Therefore, using Equation (6), we see that to maintain steady-state wind-driven accretion, the value of β_0 needs to decrease with radius as $\beta_0 \propto R^{-(0.75-0.46)/0.66} = R^{-0.44}$ for a MMSN disk. This is in accordance with our choice of smaller β_0 at larger disk radii. We will further discuss the wind-driven accretion rate based on the fitting formulas above in Section 5.2.

3.3. The Strong Current Layer

The properties of the strong current layer for most of our quasi-1D runs are given in the last three columns of Table 2. We see two very clear trends: 1). Toward outer disk radii, the strong current layer shifts toward disk midplane, becomes wider, with slower gas inflow; 2). With stronger net vertical magnetic flux, the strong current layer shifts toward disk surface, becomes sharper, with much faster gas inflow. As discussed in paper I, the strong current layer is offset from the midplane since the midplane region is too poorly coupled to the gas hence current is not permitted. It is generally located at the height where the gas starts to be partially coupled with the magnetic field. Since the gas near midplane region becomes progressively better coupled with magnetic fields, it is therefore understandable that the location of the strong current layer shifts toward disk

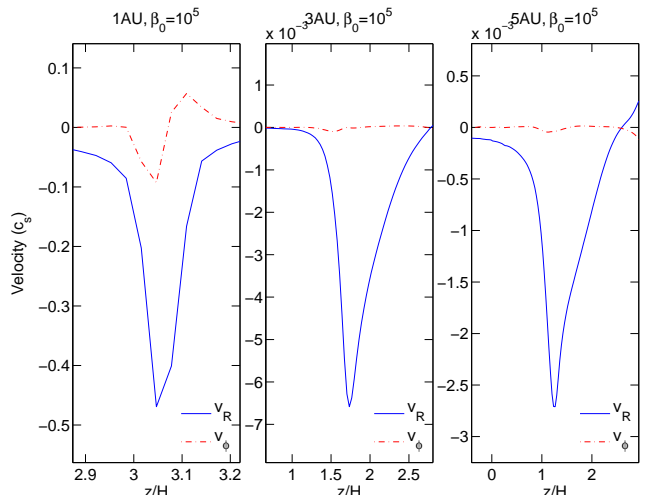


FIG. 3.— The radial (blue solid) and azimuthal (red dash-dotted) velocity profiles across the strong current layer in three quasi-1D simulation runs at 1 AU, 3 AU and 5 AU respectively, with fixed $\beta_0 = 10^5$. Note that we have rescaled the axis limits so that peak velocities are centered, and the size of each box is $4h^{SC} \times 1.5v_{R,\text{max}}^{SC}$.

midplane at larger disk radii. Also, stronger net vertical magnetic flux generates stronger toroidal magnetic field that is more difficult to flip, which favors better-coupled region (toward disk surface) to take place.

In Figure 3, we further show the radial velocity profiles across the strong current layer in the three runs at 1, 3, 5 AU with fixed $\beta_0 = 10^5$. We see that although the thickness of the strong current layers vary considerably in the three cases, their velocity profiles have very similar shapes, with sharper decrease to the midplane side (since resistivity increases). Moreover, at 5 AU, we see that the strong current layer is already very thick, and extends even to the disk midplane. This indicates that the midplane region is already partially coupled to the

TABLE 3
SUMMARY OF ALL 3D SIMULATIONS.

Run	α^{Max}	α^{Rey}	$T_{z\phi}^{\text{Max}}$	\dot{M}_w	z_b	z_A	$\alpha_{\text{turb}}^{\text{Max}}$	$\alpha_{\text{turb}}^{\text{Rey}}$
F-R3-b5	1.96×10^{-4}	8.16×10^{-6}	2.02×10^{-4}	6.95×10^{-5}	4.15	5.27	2.10×10^{-7}	2.80×10^{-6}
F-R3-b6	1.96×10^{-4}	1.47×10^{-5}	2.89×10^{-5}	8.03×10^{-6}	6.06	—	1.02×10^{-6}	4.52×10^{-6}
F-R5-b5	2.07×10^{-4}	0.96×10^{-6}	2.67×10^{-4}	9.83×10^{-5}	3.97	5.02	5.16×10^{-8}	4.86×10^{-7}
F-R5-b6	2.32×10^{-4}	2.32×10^{-5}	3.40×10^{-5}	6.33×10^{-6}	5.96	—	4.34×10^{-6}	7.56×10^{-6}
F-R10-b4	2.53×10^{-3}	6.18×10^{-5}	2.16×10^{-3}	6.85×10^{-4}	3.44	5.77	-1.24×10^{-4}	2.21×10^{-5}
F-R10-b5	2.40×10^{-3}	2.08×10^{-4}	2.25×10^{-4}	1.12×10^{-4}	6.31	—	6.41×10^{-5}	2.19×10^{-4}
F-R15-b4	3.86×10^{-3}	1.32×10^{-4}	3.32×10^{-3}	1.09×10^{-3}	3.17	6.27	3.18×10^{-4}	6.35×10^{-5}
F-R15-b5	2.63×10^{-3}	2.58×10^{-4}	2.91×10^{-4}	9.25×10^{-5}	5.88	—	7.68×10^{-5}	9.40×10^{-5}

Maxwell and Reynolds stresses α^{Max} and α^{Rey} are measured in the disk zone ($-z_b < z < z_b$), wind stresses $T_{z\phi}^{\text{Max}}$ are averaged values measured at the wind base $z = \pm z_b$. All 3D simulations eventually have odd- z symmetry. Also note that for simulations with weaker net vertical field, the Alfvén points are not contained in the simulation box.

magnetic field, and we find that in this run, the Elsasser numbers at midplane are $\Lambda \approx Am \approx 0.1$. This radius, as we shall discuss in Section 4, is close to the outer boundary of the pure laminar accretion zone.

3.4. Unsteady Runs

Among all our quasi-1D simulations, we find that three of the runs never settle into a laminar state (S-R3-b6, S-R5-b6 and S-R8-b5), which are not included in Table 2. These runs show obvious signs of time variability all the time, where all the physical quantities exhibit large amplitude variations especially in the surface layer of the disk, and mass ejection occurs episodically. We have further tried to initialize runs S-R3-b6 and S-R5-b6 from the time and horizontally averaged profiles from their 3D counterparts, while they evolve into similar situations. We therefore conclude that laminar solutions can not be found for the combination of parameters in these runs. Based on these results, we note that toward larger radii, progressively larger net vertical flux is required to obtain a steady laminar solution.

4. RESULTS: 3D SIMULATIONS

Obtaining a quasi-1D solution does not necessarily mean that the solution is stable since non-axisymmetric modes are artificially suppressed. In paper I, we have demonstrated that at 1 AU, the laminar solution remains stable in 3D simulations. In this section, we first check whether the laminar quasi-1D solutions we obtained in the previous section persist in 3D, and we further explore the gas dynamics in the outer region (up to 15 AU) to identify the transition from the pure laminar wind to the onset of the MRI. For all the 3D simulations, we show the standard diagnostic quantities in Table 3, and they will be discussed in the following subsections.

4.1. Stability of quasi-1D Results

We first consider the two 3D runs F-R3-b5 and F-R5-b5 where laminar solutions were found in quasi-1D simulations. As can be seen in Table 3, the value of essentially all their diagnostics agree very well with their quasi-1D counterparts. The 3D runs exhibit very weak level of turbulent Reynolds stress in the disk zone that is of the order 10^{-6} or less in natural unit. This level is much smaller than the level reported in Shen et al. (2006) from the decay of hydrodynamic turbulence, which leaves small amplitude linear modes in shearing-box whose amplitude is

well preserved due to the low-level numerical dissipation in the Athena code. Therefore, it is consistent with pure laminar flow. The slight difference in other measured quantities such as $T_{z\phi}^{\text{Max}}$ and \dot{M}_w between runs S-R5-b5 (even symmetry) and F-R5-b5 (odd symmetry) can be attributed to the difference in their symmetry, as one compares runs S-R3-b5a and S-R3-b5b. In sum, we confirm that the quasi-1D results discussed in Section 3 are robust in 3D.

4.2. A Fiducial Case

Results presented in Section 3 indicate that laminar solution becomes impossible at larger disk radii and smaller net vertical magnetic flux. The boundary resides at 3-5 AU for $\beta_0 = 10^6$ and ~ 8 AU for $\beta_0 = 10^5$. Correspondingly, we conduct 3D runs for these parameters (except replacing 8 AU to 10 AU). These 3D runs show qualitatively similar features in their saturated states, and here we take run F-R10-b5 as a standard example.

In Figure 4 we show the space-time plot of the horizontally averaged toroidal magnetic field \overline{B}_y and vertical kinetic energy $\log_{10}(\overline{\rho v_z^2}/2)$ for run F-R10-b5. We see that at the beginning, the system is prone to the MRI and evolves into MRI turbulence. This is most evident from the characteristic ‘‘Butterfly’’ pattern in the first ~ 40 orbits, where the mean B_y changes sign over a (quasi-) period of about 10 orbits⁴. In this initial phase, the mean toroidal field at disk midplane is very weak (comparable to net vertical field), a field geometry that is favorable for the MRI in the AD dominated regime (at disk midplane). We find that the MRI turbulence is mainly driven from the midplane region, giving rise to stress level of $\alpha_{\text{turb}} \lesssim 10^{-3}$ and is responsible for the dynamo behavior. The base of the FUV layer is also MRI-unstable, but its activity is overwhelmed by the magnetic dynamo behavior buoyantly rising from the midplane. Subsequently, the dynamo disappears, accompanied by the amplification of the mean B_y near the midplane, yet the mean B_y still undergoes a local minimum across the

⁴ This dynamo pattern is most well-known in ideal MHD simulations with zero net vertical magnetic flux, while it is also present in the presence of net vertical flux but becomes progressively less periodic with increasing net flux (Bai & Stone 2013a). The periodicity of the dynamo pattern also changes in the presence of AD (Simon et al. 2013a).

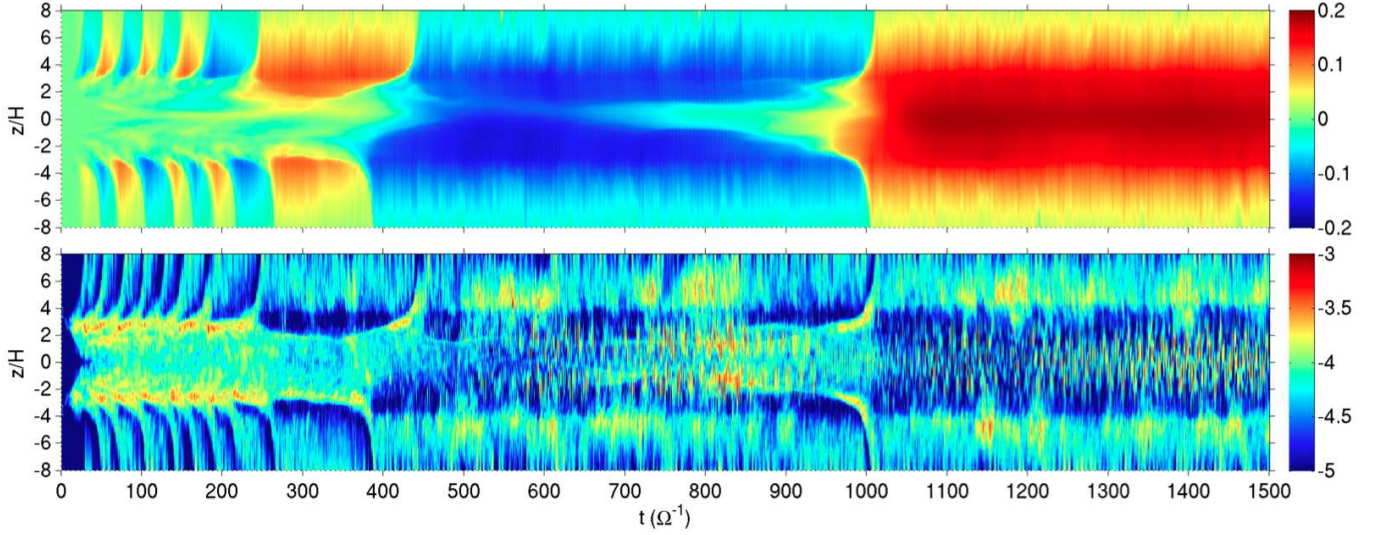


FIG. 4.— Space-time plot of horizontally averaged toroidal magnetic field \bar{B}_y (upper panel) and vertical kinetic energy $\log_{10}(\overline{\rho v_z^2}/2)$ (lower panel) for our 3D run F-R10-b5. The system reaches the final configuration after $t \approx 1000\Omega^{-1}$. See Section 4.2 for more details.

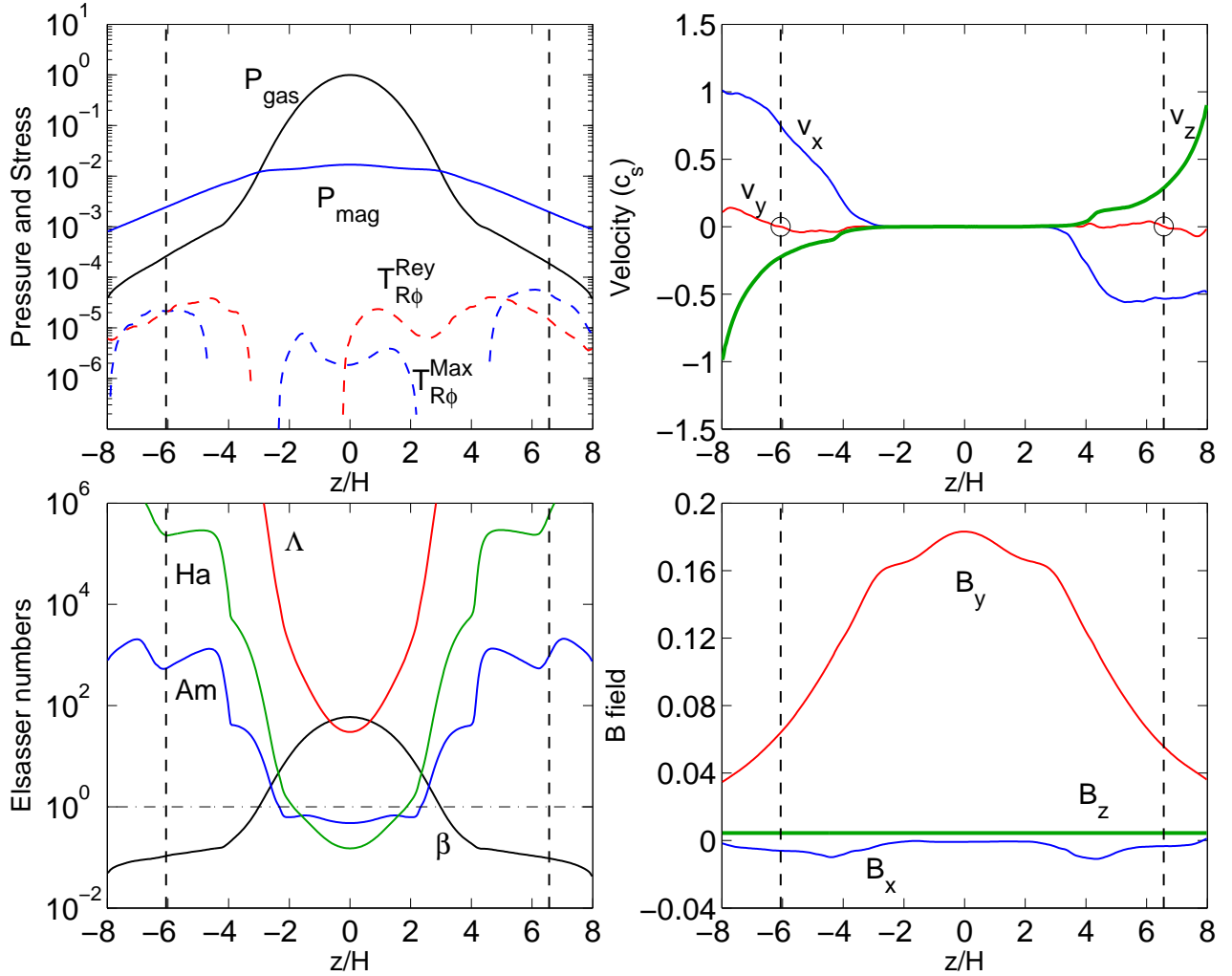


FIG. 5.— Same as Figure 1, but for 3D run F-R10-b5 at 10 AU with $\beta_0 = 10^5$. For the upper left panel, we show turbulent (rather than the full) contribution to the $R\phi$ component of Maxwell and Reynolds stresses. For the upper right panel, the Alfvén points are not shown since they are not contained in the simulation domain.

disk midplane. The system appears to be adjusting itself between $t = 200 - 1000\Omega^{-1}$, arriving at the final steady-state configuration from $t = 1000\Omega^{-1}$ on, where the mean B_y profile has a single peak at the midplane. It appears that the strength of the midplane mean B_y largely controls the turbulent activities: strong $\overline{B_y}$ leads to weaker midplane turbulence, as one compares the two panels of Figure 4. It is unclear what controls the mean toroidal field around disk midplane, but the fact that it takes the system more than 150 orbits to settle to the final state is indicative of its marginal nature on the transition from purely laminar flow to the onset of the MRI. To obtain reliable time-averaged quantities, we have run the simulation further to $t = 1500\Omega^{-1}$.

Now we focus on the final saturated state of the simulation since $t = 1080\Omega^{-1}$. From the space-time plot we see large time variabilities on ρv_z^2 take place at both midplane and the surface FUV layer, indicating turbulence is driven at both locations. The magnetic field is dominantly toroidal, and magnetic fluctuations due to turbulence are much weaker compared with the mean toroidal field, allowing us to extract time-averaged vertical profiles. In Figure 5, we show the time-averaged vertical profiles of various quantities analogous to Figure 1. The only difference is that the dashed curves on the top left panel correspond to the turbulent component of (rather than the full) $T_{r\phi}$. We observe the following features.

1). AD is the dominant non-ideal MHD effect all over the disk. It is strongest at disk midplane, and becomes weaker toward disk surface due to X-ray and FUV ionizations. Ohmic resistivity is totally negligible (with $\Lambda \gtrsim 50$).

2). Both the midplane region and the surface FUV layer show enhanced (but still weak) turbulent stress, and turbulence is largely hydrodynamical ($\alpha_{r\phi, \text{turb}}^{\text{Rey}} > \alpha_{r\phi, \text{turb}}^{\text{Max}}$). The turbulence at the FUV layer is much more vigorous since the density is much smaller compared with the midplane region.

3). An outflow is launched, but the flow velocity is much slower compared with the laminar case. The Alfvén point is not contained with the simulation box, hence the properties of the outflow may be affected more by the vertical boundary condition (e.g., the feature of the v_y profile near vertical boundary in Figure 5). We note that the Alfvén point moves away from midplane as one reduces the net vertical magnetic flux (Bai & Stone 2013a, paper I), the fact that the Alfvén point falls beyond the simulation box is consistent with smaller net magnetic flux and weaker outflow.

The MRI turbulence in the midplane region merits some more discussion. Within $|z| < 2H$, we see from Figure 5 that $Am \sim 0.5$ with a flat vertical profile, and $B_y \sim 0.18$ in code unit with a relatively flat vertical profile as well. We note that the presence of mean toroidal field significantly changes the dispersion relation of the MRI. Using the general dispersion relation derived by Kunz & Balbus (2004), we find that given these parameters, the most unstable MRI mode correspond to $2\pi/k_z \approx H - 3H$, with fastest growth rate of $0.018\Omega^{-1}$, and $k_x \approx k_z$. Therefore, the most unstable modes can be properly fitted into our simulation box. According to the simulation results from Bai & Stone (2011), under the

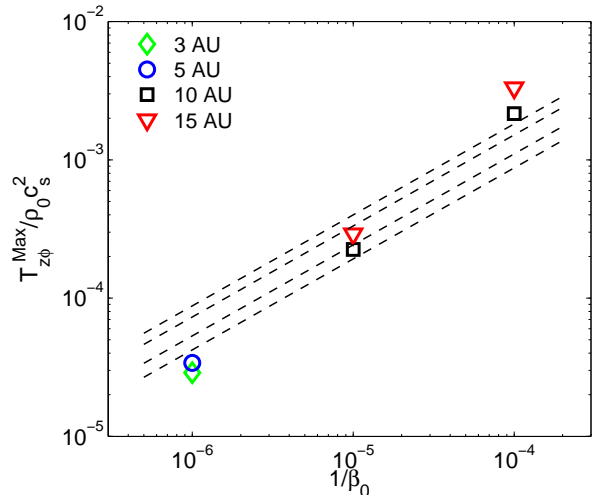


FIG. 6.— The wind stress T_{z0}^{Max} as a function of net vertical magnetic flux (characterized by β_0) measured from all our 3D simulations with midplane turbulence. Different symbols correspond to simulations at different radii. Dashed lines show the fitting formula (10) obtained from (quasi-1D) laminar wind simulations for each radii (from 3AU to 15 AU, bottom to top). All quantities are in code units. Note significant deviations from the laminar-wind fitting formula.

most favorable magnetic geometry, the resulting turbulent stress is of the order 4×10^{-3} for $Am \sim 0.5$ (see their Equations (24) and (26)). In our case, the field geometry is highly toroidal field dominated with $\overline{B_y}/\overline{B_z} \approx 40$. Note that this is close to the least favorable field geometry for Am of order unity (Bai & Stone 2011), and the low level of turbulent stress ($\lesssim 10^{-4}$, see Table 3) in the midplane is consistent with theoretical expectations⁵.

In sum, we find that in this marginal case, Ohmic resistivity becomes irrelevant and MRI operates at both disk midplane and surface FUV layer. The level of the turbulence and efficiency of turbulent angular momentum transport in the midplane is low because of a toroidal-dominated magnetic field configuration near the midplane region. The surface FUV layer is much more turbulent but is not very efficient to transport angular momentum due to its low density.

4.3. Parameter Dependence

In this subsection we discuss the rest of the 3D simulations (all except the two mentioned in Section 4.1). We start from the two runs at 3 AU and 5 AU with $\beta_0 = 10^6$. The midplane region in these two cases still has large Ohmic resistivity, hence the MRI does not operate there. However, very weak MRI turbulence is excited in the FUV layer. From Table 3, we see that the turbulent stresses are systematically larger than the two 3D companion runs with $\beta_0 = 10^5$ (i.e., laminar wind cases), indicating that MRI is in operation. This is further confirmed by looking at the MRI dispersion relation. At the FUV front (located at $z \sim \pm 4H$), the gas density in these two cases is around 5×10^{-4} . With $\beta_0 = 10^6$, the most

⁵ Here we are comparing the turbulent stress (rather than total stress) with the the unstratified simulation results of Bai & Stone (2011) because the stress due to large-scale magnetic fields in unstratified shearing-box simulations is zero.

unstable wavelength is approximately $0.5H$. Although this simple analysis ignores stratification, the relatively small wavelength indicates the viability of the MRI. However, due to the low density in the FUV layer, the resulting value of α_{turb} is extremely small ($\sim 10^{-5}$).

For the four runs at 10 AU and 15 AU, AD becomes the dominant non-ideal MHD effects throughout the disk, and MRI turbulence sets in both from the midplane and from the FUV layer. The properties of these runs at saturation are all very similar to the fiducial case F-R10-b5 discussed in detail earlier. Among them, run F-R10-b4 appears closest to the laminar case, with a negative turbulent Maxwell stress ($\alpha_{\text{turb}}^{\text{Max}}$) and also a smallest $\alpha_{\text{turb}}^{\text{Rey}}$ compared with the other three. This run is parametrically similar to our quasi-1D run S-R8-b4 where pure laminar configuration is stable. Being located slightly outward, it does show some turbulent behavior and we find that both the midplane region and the FUV layer is marginally unstable to the MRI. At this location of 10 AU, we expect a purely laminar configuration with slightly stronger net vertical flux. Similarly, we expect unambiguous MRI turbulence at larger radii with fixed β_0 , which is indeed the case as in our run F-R15-b4.

For 3D runs with MRI turbulence, we find that the scaling relations (9) and (10) no longer hold. As an example, we show in Figure 6 the wind stresses from these 3D runs and compare them with expectations from the laminar wind fitting formula. We find that in the presence of turbulence, the dependence of wind stress on net vertical magnetic flux is more steep: $T_{z\phi}^{\text{Max}}$ from runs F-R3-b6 and F-R5-b6 fall significantly from expectations, while $T_{z\phi}^{\text{Max}}$ from runs F-R10-b4 and F-R15-b4 are well above (but note the caveat that in simulations with weaker fields, the Alfvén points are not contained in the simulation box). These results set the radial range where the laminar wind fitting formulas are applicable.

We note that in all these 3D simulations, turbulence only contributes to a small fraction of the total stress $T_{r\phi}$. The dominant contribution is from the Maxwell stress due to large-scale magnetic field (i.e., magnetic breaking). Using Equation (6), we see that to have an accretion rate of $10^{-8}M_{\odot} \text{ yr}^{-1}$, the required value of α is about $4 - 5 \times 10^{-3}$ at 10 – 15 AU. From the simulations, the measured α^{Max} is a bit small but close to this level. We also note that in quasi-1D runs at inner disk radii, the level of α_{Max} at $\beta_0 = 10^4$ is also substantial. Also from 1D simulations, we see that under the physical symmetry (with field flip and a strong current layer), the value of α_{Max} is slightly smaller than (but on the same order of) the case under the unphysical odd- z symmetry. These results together suggest magnetic breaking can potentially play a non-negligible role in angular momentum transport⁶.

For a physical scenario where horizontal field flips within the disk, our quasi-1D runs have implied that at larger disk radii, the flip is likely to take place close to the midplane at large radii, and the thickness of this “strong current layer” can be large ($\gtrsim H$). If this is the case, the midplane region is likely to have very weak toroidal field,

⁶ Most likely only at $R \gtrsim 10$ AU. In the inner disk, $\beta_0 \gtrsim 10^5$ is sufficient for rapid wind-driven accretion, where contribution from α_{Max} is less than $\sim 10\%$.

and such field geometry is more favorable for the MRI turbulence in the AD dominated regime. It is likely that radial transport of angular momentum (i.e., MRI and magnetic breaking) becomes progressively important toward the outer disk, while at least up to the range of 10 – 15 AU, magnetocentrifugal wind can still play a dominant role in this process: the required level of wind stress $T_{z\phi}^{\text{Max}}$ at 10 – 15 AU is about $1.5 - 2 \times 10^{-4} \rho_c c_s^2$ (for accretion rate of $10^{-8}M_{\odot} \text{ yr}^{-1}$), which is easily accounted for with $\beta_0 = 10^5$.

5. SUMMARY AND DISCUSSIONS

5.1. Criteria for the Laminar Wind Solution

Piecing together all simulations presented in the present paper and paper I, we show in Figure 7 the parameter space we have explored, indicating whether a laminar solution is possible. Clearly, laminar solutions can be found in the inner disk less than 10 AU. The radius where turbulence sets in depends on the strength of the net vertical magnetic field. With relatively strong net vertical field $\beta_0 \sim 10^4$, the purely laminar zone could extend to about 10 AU, while for much weaker net vertical field $\beta_0 \sim 10^6$, the purely laminar zone could shrink to 3 AU. We emphasize that even though we have labeled “turbulent” in much of parameter space in Figure 7, the level of turbulence can be extremely weak. In particular, for the two symbols at 3 AU and 5 AU with $\beta_0 = 10^6$, extremely weak turbulence only exists in the the surface FUV layer, and the bulk of the disk is still largely laminar. Even at 10 AU and 15 AU, where turbulence exists at both disk midplane and the FUV layer for $\beta_0 \gtrsim 10^4$, the transport coefficient is of the order $\alpha \sim 10^{-4}$ or less.

Using Equations (6) and (10) and under the assumption that the laminar solution exists, we further draw two dash-dotted lines in Figure 7 showing the expected parameter for the disk to maintain steady state wind-driven accretion rate of 10^{-8} and $10^{-7}M_{\odot} \text{ yr}^{-1}$. It clearly shows the importance of the laminar wind solutions at the inner disks within 10 AU. Although the parameter space marked by red circles does not obey our fitting formula (10), the deviation is not substantial (see Figure 6), and we may still use the dash-dotted lines as a reference.

Combining the results with the studies in paper I, the criteria for the existence of the laminar wind solution can be readily inferred. We emphasize that we do *not* attempt to provide quantitative and general criteria for MRI suppression and wind launching. Instead, we design these criteria specifically for qualitatively understanding the launching laminar winds from PPDs, as follows.

- Strong Ohmic resistivity ($\Lambda < 1$) in the midplane region, which is necessary to suppress the MRI around disk midplane.
- Strong AD dominated disk upper layer, which is essential to suppress the MRI at disk surface.
- The presence of (not too weak) net vertical magnetic flux, otherwise the MRI does operate but works extremely inefficiently.
- Sufficient ionization beyond disk surface ($Am \gtrsim 100$), which is essential for wind mass loading.

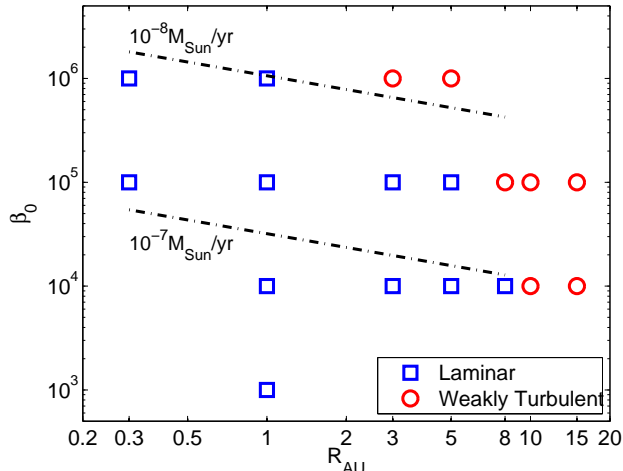


FIG. 7.— Summary of the parameter study from simulations in paper I and this paper. Each symbol denote one particular set of parameter in the $R_{\text{AU}} - \beta_0$ plane, assuming a MMSN disk model. Blue squares denote the existence of laminar wind solution, while red circles mean the disk has to be turbulent, though turbulence is very weak with stress level of the order 10^{-4} or less. Two dash-dotted lines indicate the desired β_0 as a function of radius for wind-driven accretion rate of 10^{-8} and $10^{-7} M_{\odot} \text{ yr}^{-1}$ (based on Equations (6) and (10) for MMSN disks).

We note that the dominance of AD in the disk surface layer is always the case due to the low density, while strong Ohmic resistivity at disk midplane is only possible in the inner region of PPDs. This is the essence why such laminar wind solution does not extend to the outer disk beyond 10 AU as we have confirmed in this paper. The requirement of not-too-weak magnetic field is mainly to avoid the MRI in the surface FUV layer. Since the FUV ionization penetrates deeper in the outer disk (under the assumption of constant penetration column), stronger field (measured in β_0) is required toward outer disk to suppress the MRI in the FUV layer, which explains the trend in Figure 7.

Another point of clarification again involves the magnetic field strength. It is well known that the MRI can be suppressed with sufficiently strong magnetic field with/without non-ideal MHD effects. In fact, conventional wind launching criterion which requires near-equipartition field strength is partly to avoid the MRI. In PPDs, if field strength approaches this level, other criteria outlined in this subsection would become meaningless. However, the conventional wind scenario would result in excessively strong mass loss and accretion unless the disk is substantially depleted (Combet & Ferreira 2008). Also, wind launching will be dramatically suppressed for field strength beyond equipartition (Shu et al. 2008; Ogilvie 2012). Therefore, throughout this paper, we always limit ourselves to field strength much weaker than equipartition ($\beta_0 \gg 1$). The main reason we are able to find laminar wind solution with field strength much weaker than equipartition is that we have adopted a realistic ionization profile (rather than constant Elsasser number profile), where suppression of the MRI by Ohmic dominated midplane is essential.

5.2. Magnetic Flux Distribution for Steady-State Accretion

In paper I, we have emphasized the importance of net vertical magnetic flux: it is the sufficient and necessary requirement to drive rapid accretion in the inner region of PPDs. In the outer region of PPDs (e.g., beyond 30 AU) where MRI-driven accretion is likely to dominate (Bai 2011b), the presence of net magnetic flux has also been shown to be crucial (Simon et al. 2013a,b), otherwise the MRI would simply be too inefficient. The rate of angular momentum transport due to either disk wind or the MRI depends sensitively on the amount of net vertical magnetic flux threading the disk. Therefore, the global distribution of poloidal magnetic flux in PPDs is the key to understanding the accretion process in PPDs.

Here we focus on the inner disk region with laminar accretion, and ask the question of what distribution of poloidal magnetic flux would result in steady state accretion with accretion rate consistent with observations? Our starting point is the fitting formula (10) in Section 3.2. Following the discussion in that section, we convert β_0 in the MMSN disk model to physical magnetic field strength, and further use Equation (6), to find the wind-driven accretion rate to be

$$\dot{M} \approx 0.91 \times 10^{-8} M_{\odot} \text{ yr}^{-1} R_{\text{AU}}^{1.21} \left(\frac{B_{z0}}{10 \text{ mG}} \right)^{0.93}. \quad (11)$$

We note that this formula applies only in the laminar region of the disk. Uncertainties with this formula mainly arise from the treatment FUV ionization, and the assumption of the MMSN temperature profile, but they should only introduce minor corrections (recall from Table 4 of paper I, varying the FUV penetration depth by a factor of 10 leads to difference in $T_{z\phi}^{\text{Max}}$ by a factor of about 2).

Clearly, this formula shows that large-scale poloidal field strength of about 10 mG at 1 AU is needed to drive accretion with the typical observed rate of $10^{-8} M_{\odot} \text{ yr}^{-1}$. We emphasize that surface density does not enter the formula above, a result identified in paper I, and sustaining steady-state accretion requires that the radial distribution of net vertical magnetic field follows $B_z(R) \propto R^{-1.3}$. In other words, using $\Phi_p(R)$ to denote the total poloidal magnetic flux contained within disk radius R , it should follow the law of $\Phi_p(R) \propto R^{0.7}$.

Questions remain regarding the transport of poloidal magnetic flux in PPDs: how can poloidal magnetic flux be arranged to arrive at the desired configuration. Most studies on magnetic flux transport in accretion disks assume balance between advection due to viscous accretion and diffusion due to resistivity (Lubow et al. 1994; Guilet & Ogilvie 2012). This is not the case for wind-driven accretion. As was discussed in paper I, the solutions obtained in our simulations has zero toroidal electric field, corresponding to a stationary magnetic flux distribution. In other words, inward advection due to wind-driven accretion is balanced exactly by the outward diffusion in the strong current layer. Although this is mainly a consequence of the shearing-box approach, such stationary magnetic flux distribution is desirable property of the wind solution. We note that other wind solutions are still possible with non-zero advection ve-

locity of magnetic flux, which generally require global approach.

5.3. Global Picture

Simulations from our paper I demonstrated a robust result that the MRI is likely to be suppressed in the inner region of PPDs, while magnetocentrifugal wind can be launched due to the large-scale poloidal magnetic flux threading the disk. Compiling further from all simulations presented in this paper, which cover a much wider range of disk radii, a new global picture on the accretion process in PPDs emerges. This new scenario is illustrated schematically in Figure 8, which contrasts with the conventional picture of layered accretion (Gammie 1996, see also Figure 7 of Armitage 2011).

Overall, the PPD can be divided into three bulk regions.

- The innermost region (region I), where the gas is sufficiently hot ($T \gtrsim 10^3\text{K}$) to thermally (collisionally) ionize Alkali metals (Na and K). The gas behaves in the ideal MHD regime, and the entire disk is highly turbulent due to the MRI.
- The inner region (region II), where the disk is largely laminar due to the combined effects of Ohmic resistivity and AD. Angular momentum transport is dominantly driven by the magnetocentrifugal wind, and accretion proceeds through a strong current layer that is offset from disk midplane.
- The outer region (region III), where MRI is likely to be the dominant mechanism for angular momentum transport, but its strength is relatively weak due to strong AD.

Below we briefly discuss each region separately, as well as the transition between them.

In region I, the gas dynamics can be inferred from ideal-MHD shearing-box simulations of the MRI. We note that since net vertical magnetic flux is essential for driving rapid accretion for other parts (regions II and III) of the disks, such net vertical flux is also likely to be present in the innermost region of the disk. Moreover, since this region is close to the star, it can also be threaded with some stellar magnetic flux. The behavior of the MRI in the presence of net vertical flux in the ideal MHD regime has recently been explored in great detail (Suzuki & Inutsuka 2009; Fromang et al. 2012; Bai & Stone 2013a). It was found that an outflow is always launched, which is highly unsteady and its mass outflow rate increases with net vertical flux similar to our laminar wind case. However, it was argued that the outflow launched from an MRI-turbulent disk is unlikely to be *directly* connected to a global wind either due to the MRI dynamo or symmetry issues (Bai & Stone 2013a). Moreover, strong interaction with the protostellar magnetosphere is also expected in the inner part of region I, which also likely launches powerful and highly dynamic outflows (Romanova et al. 2009). Therefore, we use dashed arrows in Figure 8 to illustrate such unsteady outflow whose fate remains to be explored.

The outer boundary of region I lies where the temperature drops below about 10^3K . Within region I, viscous heating is generally the dominant heating source, and for typical accretion rate of $10^{-8}M_{\odot}\text{yr}^{-1}$, the location where T drops below 10^3K is around 0.3 AU (e.g., Figure 2 of Armitage 2011, yet the exact location depends on model parameters). Since thermal ionization depends extremely sensitively on temperature near the threshold, the transition from region I to region II should be abrupt, yet it would be very interesting to explore the gas dynamics near the interface connecting the fully turbulent region and the full laminar region.

Region II has been discussed extensively in paper I and this paper. It covers the radial range where the four criteria identified in Section 5.1 are met, and extends from the outer boundary of region I to some outer radius. We note that at 3 – 5 AU, the disk wind is sufficient to drive rapid accretion at 3 – 5 AU even with weak field $\beta_0 = 10^6$. Although the thin FUV surface layer is expected to be weakly turbulent, the bulk of the disk can still be considered to be largely laminar. Therefore, we may relax our criterion 3 (of Section 5.1) and consider region II to extend to an outer radius of somewhere between 5-10 AU.

Slightly beyond the outer boundary of region II where Ohmic resistivity becomes unimportant, MRI starts to operate at disk midplane. However, because of strong AD and relatively strong toroidal-dominated magnetic field configuration near midplane, turbulence resulting from the MRI is very weak. While magnetic breaking due to large-scale radial and toroidal fields could play a non-negligible role on angular momentum transport, magnetocentrifugal wind is still most likely the dominant mechanism to drive disk accretion, provided an even- z symmetry continues to apply. The wind stress and mass loss rate no longer follow the scaling relations (Equations (9) and (10)) identified for the laminar wind region (region II) due to the presence of MRI turbulence at disk midplane and FUV layer.

Region III is not covered in our numerical simulations. However, earlier works suggest that MRI alone is capable of driving rapid accretion to feed the inner disk if under a favorable magnetic field geometry and with the assistance of tiny grains and/or FUV ionization (Bai 2011b; Perez-Becker & Chiang 2011b). Here, favorable field geometry refers to the magnetic configuration with both net vertical and mean toroidal magnetic fields, with the toroidal component a few times stronger (Bai & Stone 2011). Recently, Simon et al. (2013a,b) explored the gas dynamics in region III with shearing-box simulations. They focused at two disk radii, 30 AU and 100 AU, and found that 1) net vertical magnetic flux is essential to drive rapid accretion, 2) the MRI-driven accretion rate is a strong function of net vertical magnetic flux. There is also outflow from the simulations as a natural consequence of net vertical flux. While the fate of the outflow is again uncertain for reasons similar to that in region I, MRI is the dominant source of angular momentum transport.

It is very likely that there is a transition zone that covers a relatively wide range of radii between region II and region III (e.g., from $\sim 5 - 10\text{AU}$ to $\sim 30\text{AU}$), where the dominant angular momentum transport mechanism

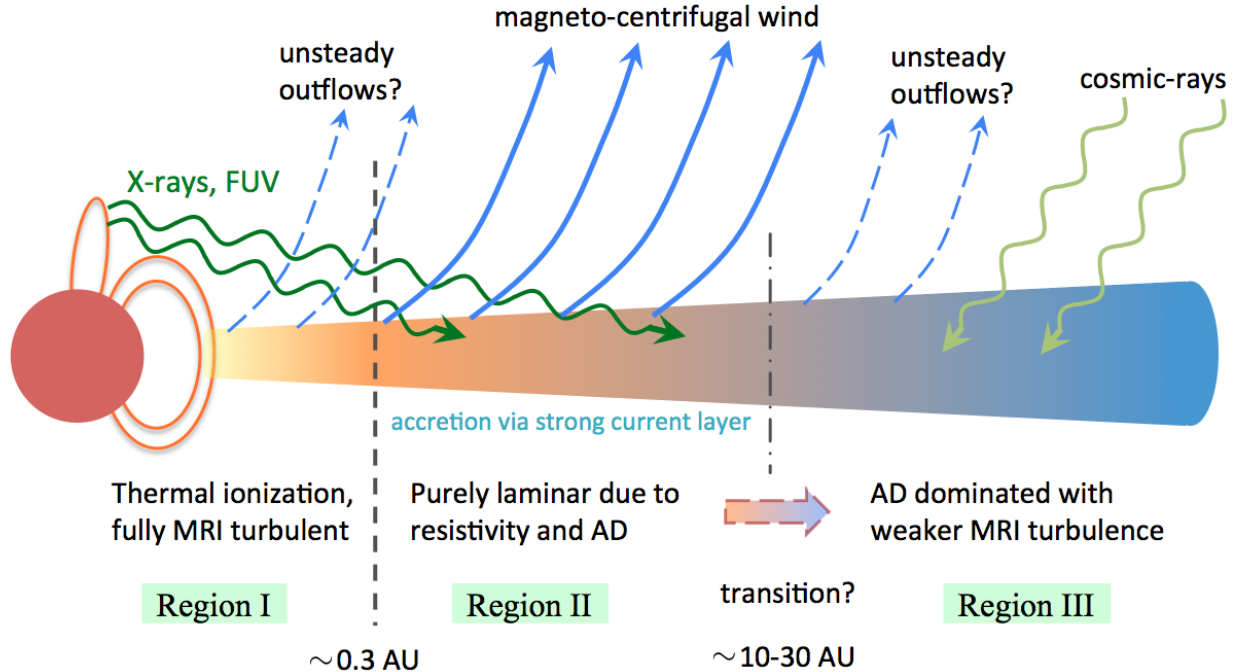


FIG. 8.— Schematic global picture of protoplanetary disks (not to the scale) in light of our new simulation results that incorporate the effect of AD. See Section 5.3 for detailed discussions.

shifts *gradually* from disk wind to the MRI/magnetic braking. Moreover, the Hall effect, which is not included in our studies, is the dominant non-ideal MHD effect in such transition radii. It will be extremely interesting to explore the transition using global simulations.

5.4. Concluding Remarks

Our simulations have demonstrated the magnetocentrifugal wind is an essential ingredient for driving accretion in the inner region of PPDs. Although we are unable to provide large-scale kinematics of the disk wind based on our local shearing-box simulations, the range of radii where we expect such disk wind is consistent with the inferred launching radii of the low-velocity component of the molecular outflows from observations (Anderson et al. 2003; Coffey et al. 2004, 2007). The laminar nature of the gas flow in the inner disk has important implications on grain growth in PPDs, planetesimal formation, and potentially planet migration, which all merit future investigations.

The global picture proposed in this paper represents a

large-scale framework, while the details of the picture remain to be explored with a lot more efforts. In particular, the Hall effect that was not included in our simulations is the dominant non-ideal MHD effect in a large portion of parameter space in PPDs and may play an important role on the MHD stability of the disk. Moreover, global simulations are essential to address the stability of the strong current layer, the transition between regions I, II and III outlined in the previous subsection, and the transport of large-scale poloidal magnetic flux. Global simulations are also necessary to quantify the kinematics of the disk wind, such as the rate and velocity of the mass outflow, and to make direct comparisons with observations.

I thank the referee for useful comments and suggestions that improve the clarity of this paper. This work is supported for program number HST-HF-51301.01-A provided by NASA through a Hubble Fellowship grant from the Space Telescope Science Institute awarded to XN.B, which is operated by the Association of Universities for Research in Astronomy, Incorporated, under NASA contract NAS5-26555.

REFERENCES

- Anderson, J. M., Li, Z.-Y., Krasnopolsky, R., & Blandford, R. D. 2003, *ApJ*, 590, L107
- Arce, H. G., Shepherd, D., Gueth, F., Lee, C.-F., Bachiller, R., Rosen, A., & Beuther, H. 2007, *Protostars and Planets V*, 245
- Armitage, P. J. 2011, *ARA&A*, 49, 195
- Bacciotti, F., Ray, T. P., Mundt, R., Eisloffel, J., & Solf, J. 2002, *ApJ*, 576, 222
- Bai, X.-N. 2011a, *ApJ*, 739, 50
- . 2011b, *ApJ*, 739, 51
- Bai, X.-N. & Goodman, J. 2009, *ApJ*, 701, 737
- Bai, X.-N. & Stone, J. M. 2011, *ApJ*, 736, 144
- . 2013a, *ApJ*, 767, 30
- . 2013b, *ApJ*, 769, 72
- Balbus, S. A. & Hawley, J. F. 1991, *ApJ*, 376, 214
- Blandford, R. D. & Payne, D. G. 1982, *MNRAS*, 199, 883
- Cabrit, S. 2007a, *IAU Symposium*, 243, 203
- Cabrit, S. 2007b, in *Lecture Notes in Physics*, Berlin Springer Verlag, Vol. 723, ed. J. Ferreira, C. Dougados, & E. Whelan, 21
- Cabrit, S., Edwards, S., Strom, S. E., & Strom, K. M. 1990, *ApJ*, 354, 687
- Cabrit, S., Pety, J., Pesenti, N., & Dougados, C. 2006, *A&A*, 452, 897
- Cerqueira, A. H., Velázquez, P. F., Raga, A. C., Vasconcelos, M. J., & de Colle, F. 2006, *A&A*, 448, 231
- Chrysostomou, A., Bacciotti, F., Nisini, B., Ray, T. P., Eisloffel, J., Davis, C. J., & Takami, M. 2008, *A&A*, 482, 575

- Coffey, D., Bacciotti, F., & Podio, L. 2008, *ApJ*, 689, 1112
- Coffey, D., Bacciotti, F., Ray, T. P., Eisloffel, J., & Woitas, J. 2007, *ApJ*, 663, 350
- Coffey, D., Bacciotti, F., Woitas, J., Ray, T. P., & Eisloffel, J. 2004, *ApJ*, 604, 758
- Combet, C., & Ferreira, J. 2008, *A&A*, 479, 48
- Fendt, C., & Sheikhezami, S. 2013, *ApJ*, submitted (arXiv:1305.1263)
- Ferreira, J., & Pelletier, G. 1995, *A&A*, 295, 807
- Fromang, S., Latter, H. N., Lesur, G., & Ogilvie, G. I. 2012, *A&A*, 552, A71
- Gammie, C. F. 1996, *ApJ*, 457, 355
- Guilet, J. & Ogilvie, G. I. 2012, *MNRAS*, 424, 2097
- Hartigan, P., Edwards, S., & Ghandour, L. 1995, *ApJ*, 452, 736
- Hartigan, P., Edwards, S., & Pierson, R. 2004, *ApJ*, 609, 261
- Hartmann, L., Calvet, N., Gullbring, E., & D'Alessio, P. 1998, *ApJ*, 495, 385
- Hirth, G. A., Mundt, R., & Solf, J. 1997, *A&AS*, 126, 437
- Königl, A., Salmeron, R., & Wardle, M. 2010, *MNRAS*, 401, 479
- Kunz, M. W. & Balbus, S. A. 2004, *MNRAS*, 348, 355
- Li, Z.-Y. 1995, *ApJ*, 444, 848
- . 1996, *ApJ*, 465, 855
- Lubow, S. H., Papaloizou, J. C. B., & Pringle, J. E. 1994, *MNRAS*, 267, 235
- Mohanty, S., Ercolano, B., & Turner, N. J. 2013, *ApJ*, 764, 65
- Ogilvie, G. I. 2012, *MNRAS*, 423, 1318
- Perez-Becker, D. & Chiang, E. 2011a, *ApJ*, 727, 2
- . 2011b, *ApJ*, 735, 8
- Pyo, T.-S., Kobayashi, N., Hayashi, M., Terada, H., Goto, M., Takami, H., Takato, N., Gaessler, W., Usuda, T., Yamashita, T., Tokunaga, A. T., Hayano, Y., Kamata, Y., Iye, M., & Minowa, Y. 2003, *ApJ*, 590, 340
- Ray, T., Dougados, C., Bacciotti, F., Eisloffel, J., & Chrysostomou, A. 2007, *Protostars and Planets V*, 231
- Romanova, M. M., Ustyugova, G. V., Koldoba, A. V., & Lovelace, R. V. E. 2009, *MNRAS*, 399, 1802
- Salmeron, R., Königl, A., & Wardle, M. 2011, *MNRAS*, 412, 1162
- Sano, T. & Stone, J. M. 2002a, *ApJ*, 570, 314
- . 2002b, *ApJ*, 577, 534
- Shakura, N. I. & Sunyaev, R. A. 1973, *A&A*, 24, 337
- Shang, H., Li, Z.-Y., & Hirano, N. 2007, *Protostars and Planets V*, 261
- Shen, Y., Stone, J. M., & Gardiner, T. A. 2006, *ApJ*, 653, 513
- Shu, F., Najita, J., Ostriker, E., Wilkin, F., Ruden, S., & Lizano, S. 1994, *ApJ*, 429, 781
- Shu, F. H., Lizano, S., Galli, D., Cai, M. J., & Mohanty, S. 2008, *ApJ*, 682, L121
- Soker, N. 2005, *A&A*, 435, 125
- Simon, J. B., Bai, X.-N., Stone, J. M., Armitage, P. J., & Beckwith, K. 2013a, *ApJ*, 764, 66
- Simon, J. B., Bai, X.-N., Armitage, P. J., Stone, J. M., & Beckwith, K. 2013b, *ApJ*, in preparation
- Stone, J. M., Gardiner, T. A., Teuben, P., Hawley, J. F., & Simon, J. B. 2008, *ApJS*, 178, 137
- Suzuki, T. K. & Inutsuka, S.-i. 2009, *ApJ*, 691, L49
- Wardle, M. 1997, in *Astronomical Society of the Pacific Conference Series*, Vol. 121, IAU Colloq. 163: Accretion Phenomena and Related Outflows, ed. D. T. Wickramasinghe, G. V. Bicknell, & L. Ferrario, 561
- Wardle, M. & Koenigl, A. 1993, *ApJ*, 410, 218
- Wardle, M. & Salmeron, R. 2012, *MNRAS*, 422, 2737
- Weidenschilling, S. J. 1977, *MNRAS*, 180, 57
- Woitas, J., Ray, T. P., Bacciotti, F., Davis, C. J., & Eisloffel, J. 2002, *ApJ*, 580, 336
- Woodall, J., Agúndez, M., Markwick-Kemper, A. J., & Millar, T. J. 2007, *A&A*, 466, 1197